

Synthesis, Structural Characterization and Physical Properties of the New Transition Metal Oxyselenide $\text{Ce}_2\text{O}_2\text{ZnSe}_2$

Chris M. Ainsworth,[†] Chun-Hai Wang,[†] Matthew G. Tucker,[‡] John S. O. Evans^{*,†}

[†]Department of Chemistry, University Science Site, Durham University, South Road, Durham, DH1 3LE, United Kingdom

[‡]ISIS Neutron and Muon Source, Science and Technology Facilities Council, Rutherford Appleton Laboratory, Harwell, Oxford, Didcot, UK, OX11 0QX

KEYWORDS. oxychalcogenides, mixed-anion, semiconductor, magnetism, powder diffraction, crystallography.

ABSTRACT: The quaternary transition metal oxyselenide $Ce_2O_2ZnSe_2$ has been shown to adopt a ZrCuSiAs-related structure with Zn^{2+} cations in a new ordered arrangement within the $[ZnSe_2]^{2-}$ layers. The color of the compound changes as a function of cell volume, which can vary by $\sim 0.4\%$ under different synthetic conditions. At the highest, intermediate and lowest cell volumes the color is yellow-ochre, brown and black respectively. The volume decrease is attributed to oxidation of the Ce from +3 to +4, the extent of which can be controlled by the synthetic conditions. $Ce_2O_2ZnSe_2$ is a semiconductor at all cell volumes with experimental optical band gaps of 2.2, 1.4 and 1.3 eV for high, intermediate and low cell volume samples respectively. SQUID measurements show $Ce_2O_2ZnSe_2$ to be paramagnetic from 2–300 K with a negative Weiss temperature of $\theta = -10$ K suggesting weak antiferromagnetic interactions.

INTRODUCTION

Since the 2008 discovery of superconductivity at ~ 26 K in F doped LaOFeAs,¹ there has been extensive study of mixed anion materials. Recently superconductivity has been reported in structurally related oxychalcogenides such as $Bi_4O_4S_3$ (T_c up to 8.6 K),²⁻⁴ $LnO_{1-x}F_xBiS_2$ ($Ln = La, Ce, Pr, Nd, Yb$) (T_c 1.9–4.5 K)⁵ and $LaO_{0.5}F_{0.5}BiSe_2$ (T_c 2.6 K).⁶ Issues with sample purity have led to some controversy over the superconducting phase in these systems with $Bi_3O_2S_3$ suggested as the superconducting phase in the $Bi_4O_4S_3$ system.^{7,8} Superconductivity aside, many oxychalcogenides have other interesting electronic, magnetic and optical properties. For example, LaCuOS is a wide band gap p-type semiconductor with an optical band gap of 3.1 eV, and can be acceptor-doped to give room-temperature conductivity up to $2.6 \times 10^{-1} S cm^{-1}$.⁹

LaCuOS and analogous $LnOCuCh$ ($Ln = La-Nd, Bi; Ch = S, Se, Te$) materials adopt the tetragonal ZrCuSiAs structure, space group $P4/nmm$. The structure is built up from alternating layers of fluorite-like $[Ln_2O_2]^{2+}$ sheets and antiferrofluorite-like $[Cu_2Ch_2]^{2-}$ sheets.^{10,11} There has been recent interest in compounds related to $LnOCuCh$ with divalent

transition metal ions. This divalency leads to half occupancy of the transition metal sites giving $[MSe_2]^{2-}$ layers, the ordering of which can be complex. The first of these materials, $Ce_2O_2MnSe_2$, was reported as having random 50% statistical occupancy of Mn on each site.¹² This arrangement retains the tetragonal space group $P4/nmm$, of $LnOCuCh$ -type compounds. Other work in our group shows that this random distribution is incorrect, however the $P4/nmm$ structure provides a useful parent or “subcell” model in which to initially identify ZrCuSiAs-related compounds, and from which to consider the structural relationships between materials. $Ce_2O_2FeSe_2$ has $[FeSe_2]^{2-}$ layers containing 1-D chains of exclusively edge-sharing, E, (stripe-like) $FeSe_4$ tetrahedra,¹³ while $La_2O_2CdSe_2$ has $[CdSe_2]^{2-}$ layers containing exclusively corner-sharing, C, (checkerboard-like) $CdSe_4$ tetrahedra.¹⁴ $La_2O_2ZnSe_2$ has $[ZnSe_2]^{2-}$ layers containing sections of both stripe-like edge-sharing $ZnSe_4$ tetrahedra, and checkerboard-like corner-sharing $ZnSe_4$ tetrahedra.¹⁵ It can therefore be considered as an intermediate structure between $Ce_2O_2FeSe_2$ and $La_2O_2CdSe_2$. These different ordering patterns are illustrated in Figure 1.

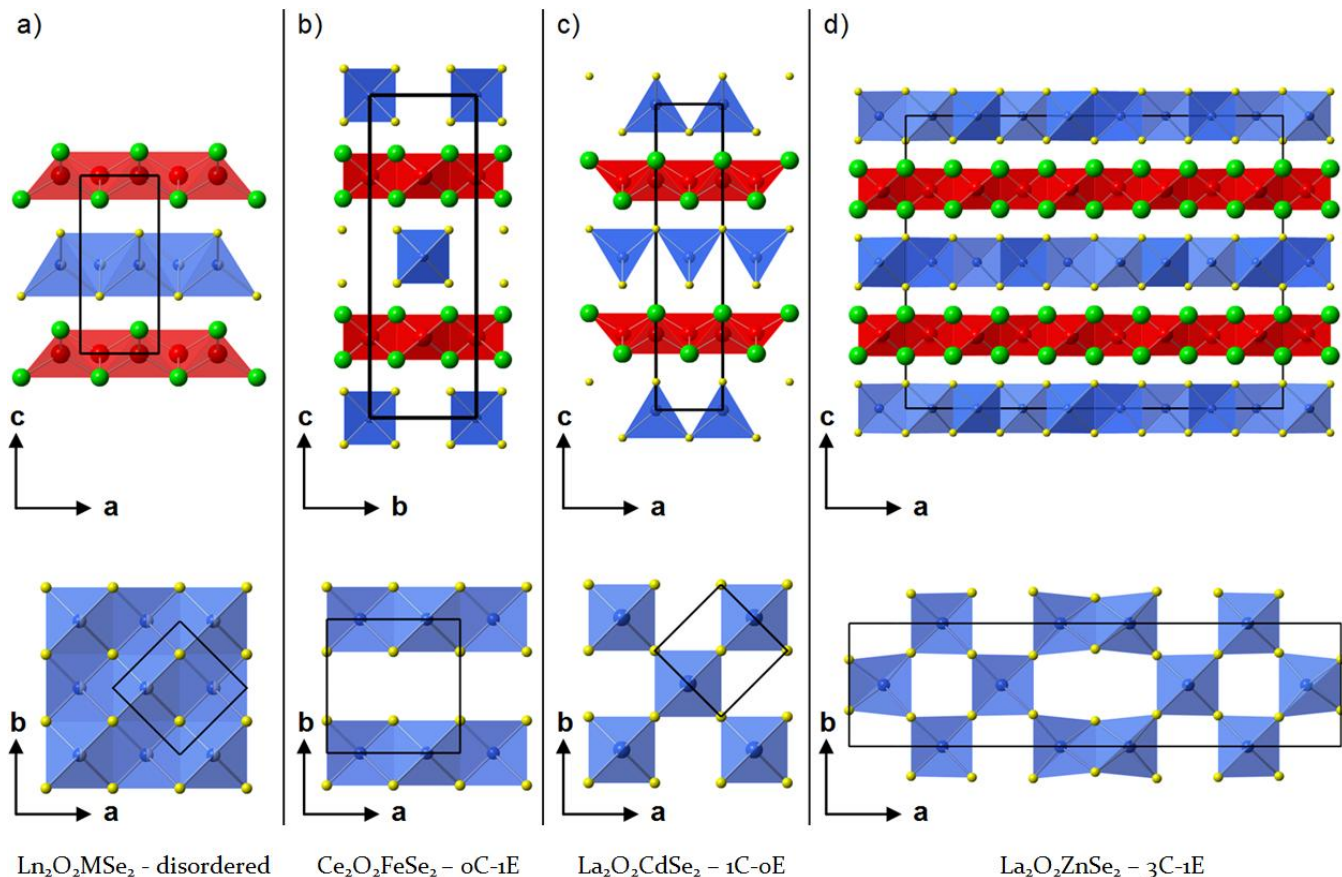


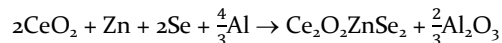
Figure 1. ZrCuSiAs-derived structures reported for (a) $\text{Ln}_2\text{O}_2\text{MSe}_2$, $P4/nmm$ symmetry (b) $\text{Ce}_2\text{O}_2\text{FeSe}_2$, $Imcb$ symmetry (c) $\text{La}_2\text{O}_2\text{CdSe}_2$, $P4_2/nmc$ symmetry (d) $\text{La}_2\text{O}_2\text{ZnSe}_2$, $Bmab$ symmetry. Top figures show the fluorite-like sheets of edge-sharing Ln_2O tetrahedra (red) and antifluorite-like sheets of MSe_4 tetrahedra (blue). Bottom figures are the view down $[001]$, showing the arrangement of MSe_4 tetrahedra. Ln^{3+} cations are shown in green, O^{2-} anions in red, M^{2+} cations in blue and Se^{2-} anions in yellow.

We report here the synthesis and characterization of the new transition metal oxyselenide $\text{Ce}_2\text{O}_2\text{ZnSe}_2$, which displays different structural and physical properties dependant on the synthetic conditions. Structural characterization indicates that the Zn^{2+} cations display a novel ordering pattern within the $[\text{ZnSe}_2]^{2-}$ layers. The structure was determined by first establishing the unit cell volume by electron diffraction and Pawley fitting of X-ray powder diffraction (XRPD) data, followed by symmetry-adapted distortion mode analysis to determine the Zn^{2+} ordering pattern. This is complemented by neutron powder diffraction data. Diffuse reflectance measurements show that $\text{Ce}_2\text{O}_2\text{ZnSe}_2$ is a semiconductor, though the bandgap is dependent on the synthetic conditions. SQUID measurements show $\text{Ce}_2\text{O}_2\text{ZnSe}_2$ to be paramagnetic from 2–300 K.

EXPERIMENTAL SECTION

Polycrystalline samples of $\text{Ce}_2\text{O}_2\text{ZnSe}_2$ were prepared by reaction of CeO_2 (99.99%, Alfa Aesar, heated to 1000 °C before use), Zn (99.9%, Sigma Adrich) and Se (99.999%, Alfa Aesar) powders in a 1:2:1 ratio. Reagents were intimately ground and placed in an alumina crucible. Al powder (99.5% Alfa Aesar) was placed in a second alumina crucible to act as an oxygen getter (forming Al_2O_3 during the reaction). These two crucibles were placed in an evacuated ($<10^{-3}$ atm) silica tube and slowly heated to a final dwell temperature for a set

time before cooling to room temperature. The equation for the reaction is:



The effect of final dwell temperature was investigated at 1100, 1150, 1175, 1200 and 1225 °C, with the final dwell time fixed at 12 h and aluminum oxygen getter (AOG) molar amount fixed at 110% (i.e. a 10% molar excess). The effect of final dwell time was investigated by holding at 1200 °C for 1, 3, 6, 9, 12 and 24 h with 110% AOG. The effect of the AOG quantity was investigated by using molar amounts of 90, 95, 100, 105 and 110% at 1200 °C for 12 h. In each case 0.6 g of sample was prepared.

For neutron powder diffraction (NPD) experiments at ISIS, a large sample (~2.4 g) was made by synthesizing four 0.6 g samples at 1200 °C, with a 12 h dwell time and 110% AOG. These four samples were then intimately ground together and reheated for 12 h at 1200 °C in an evacuated quartz tube containing 0.002 g of Se. This synthesis method was preferred for the neutron sample as it contained only a single impurity phase (~5% $\text{Ce}_2\text{O}_2\text{Se}$) and gave a low cell volume sample with superstructure peaks that could be indexed on a commensurate unit cell. Experimental warning: attempts to synthesize more than 0.6 g at 1200 °C (where silica starts to soften) in a single tube can lead to the tube swelling and ultimately bursting.

X-ray powder diffraction (XRPD) data were collected using a Bruker D8 diffractometer operating in reflection mode with $\text{Cu K}\alpha_{1/2}$ radiation, Lynxeye Si strip PSD, step size 0.02° and

variable slits. Samples were sprinkled onto Si zero-background slides covered with a thin layer of Vaseline. For initial phase identification and cell parameter determination, room-temperature data were collected for 30 min over a 2θ range 8–120°. Where more detailed structural information and/or XRPD patterns are presented, room temperature data were (unless specified otherwise) collected for 14 h over a 2θ range 8–120°. NPD data for Rietveld analysis were collected on the GEM diffractometer at ISIS. A ~2.4 g sample was loaded into a 6 mm diameter cylindrical vanadium can and data acquired for 2 h at room temperature. Powder diffraction data were analysed by the Rietveld method¹⁶ using the Topas Academic (TA) software.¹⁷⁻¹⁹ A combined X-ray and neutron (6 detector banks) refinement was carried out using room-temperature scans. The background (shifted Chebyshev), sample height (DIFA/DIFC/ZERO for neutron refinements), peak profiles, a March Dollase unidirectional preferred orientation correction²⁰ along 001 (X-ray only), a Pitschke surface roughness correction,²¹ lattice parameters, atomic positions, isotropic thermal parameters, absorption correction, and a phase fraction of the Ce₂O₂Se impurity phase (~5 wt%) were refined.

Selected area electron diffraction (SAED) data were collected using a Jeol 2100F transmission electron microscope operating at 200 keV. The sample was deposited onto a holey carbon grid. This was mounted in a double-tilt sample holder and zone axis diffraction patterns were acquired using a Gatan Orius CCD camera.

Diffuse reflectance spectra were obtained by illumination of samples using an Energetiq LDLS EQ-99 broadband lamp and collected at 20° to the excitation using Ocean Optics software; integration times were adjusted to afford maximum response of the spectrometer without saturating the detector. NaCl was used as a reference. Data were used to calculate the reflectance spectra R(I) and then analyzed using the Kubelka-Munk treatment.^{22,23}

Magnetic measurements were carried out using a Quantum Design SQUID magnetometer in the temperature range 2–300 K on samples (c.a. 0.1 g) mounted in gelatin capsules. During the measurement, a 1000 Oe field was applied.

RESULTS & DISCUSSION

Synthesis and Phase Purity

Samples of Ce₂O₂ZnSe₂ were initially synthesized for 12 h with an AOG molar amount of 110% at 1100 °C, 1150 °C, 1175 °C, 1200 °C and 1225 °C. XRPD data showed a ZrCuSiAs-related phase had formed in varying amounts with a unit cell with $a \approx 4.01$ Å, $c \approx 8.86$ Å (the subcell), explaining the main peaks in the XRPD pattern. Weak additional reflections were observed at low angles (see Figure S11 of Supporting Information) which could not be attributed to known impurity phases. It is shown below that these are due to a superstructure. The highest phase purity was obtained at 1200 °C, as shown in Figure 2a. The purest samples were yellow-ochre in color, whilst the least pure sample changed from red to black on standing in air. This is consistent with the oxidation of the impurity phase of red Ce₂O₂Se to black Ce₂O_{2+x}Se.²⁴

Attempts were made to increase the phase purity by varying the final dwell time, while maintaining the AOG molar amount at 110% and dwell temperature at 1200 °C, Figure 2b.

Above 3 h the dwell time makes little difference, producing samples of similar phase purity, all yellow-ochre in color.

The effect of reducing the AOG molar ratio was also investigated at 1200 °C, Figure 2c. Phase purity is consistent (~97 wt%) between 110% and 100% AOG, and then drops at 95% and 90%. One important aspect of this experiment is the generation of different minor impurity phases with varying AOG, as emphasized in the inset of Figure 2c. At 110% and 105% AOG, Ce₂O₂Se is the only impurity produced and has Ce in the 3+ oxidation state. Below 105% AOG the Ce₂O₂Se amount decreases and is replaced by Ce₄O₄Se₃ and CeO₂, where Ce is in a +3/+4 and +4 oxidation state respectively, and ZnSe. The increase in the oxidation state of Ce in these impurities is likely to be due to the increase in oxygen available when the AOG falls below the stoichiometric ratio.

During the synthesis a small amount of an orange crystalline material (estimated at <0.005 g, 0.8% of the starting reagent mass) was typically observed on the quartz tube; XRPD revealed it to be ZnSe. This explains why the expected ZnSe impurity is often not present in the XRPD pattern when a small Ce₂O₂Se impurity is present.

Effects of Synthetic Conditions on Structural and Physical Properties

In addition to influencing phase purity, the AOG quantity has a significant influence on the properties of the target phase. Figure 3 shows the colours of the samples, which correlate with the unit cell volume derived by powder diffraction. Figure 4a shows the effect of final dwell temperature on cell volume. All samples have a similar cell volume, and the same yellow-ochre color (disregarding samples made at 1100 °C and 1150 °C where the phase purity is low). Figure 4b shows the effect of final dwell time on cell volume. As before, all samples have a similar cell volume and the same yellow-ochre color (disregarding the 1 h sample). Figure 4c shows the effect of the AOG quantity. This has a large effect on cell volume, and the change is accompanied by a gradual change in color, with samples being yellow-ochre, brown and black at high, intermediate and low-cell volume respectively. At 90% AOG the cell volume has increased relative to the 95% AOG sample, which is against the trend. Figure 2c suggests that at this low AOG ratio, the production of more oxidized impurity phases is favored over changes in the target phase. The sample made for PND measurements (see below) was black and had a cell volume of 2848.7(6) Å³. This is comparable to the lowest cell volume sample prepared with 95% AOG, as indicated by the red arrow in Figure 4c.

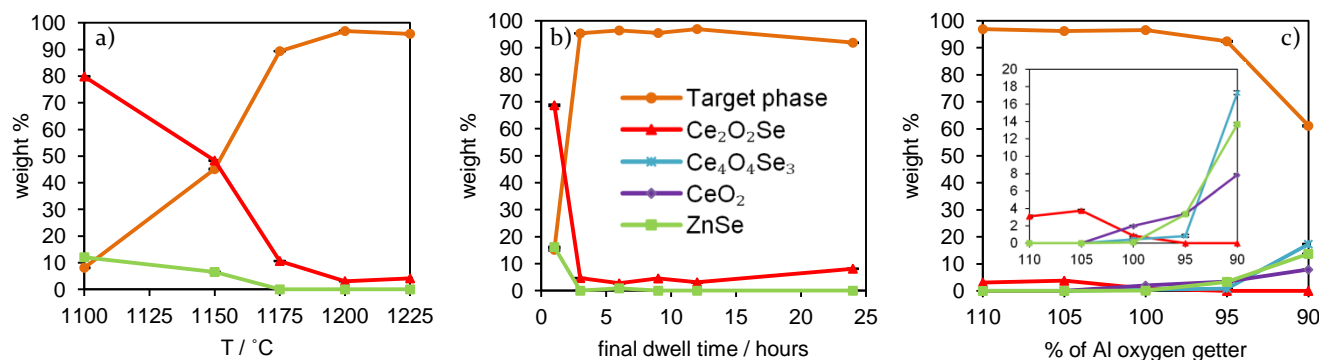


Figure 2. (a) Effect of temperature on the weight % of $\text{Ce}_2\text{O}_2\text{ZnSe}_2$ formed, with the time and AOG molar amount fixed at 12 h and 110% respectively. (b) Effect of dwell time on the $\text{Ce}_2\text{O}_2\text{ZnSe}_2$ weight fraction (1200 °C and 110% AOG). (c) Effect of AOG molar ratio on $\text{Ce}_2\text{O}_2\text{ZnSe}_2$ weight % (1200 °C, 12 h); inset: y-scale from 0-20% to show impurity phase weight fractions more clearly. Rietveld error bars are hidden by data points. More realistic error bars are around $\pm 2\%$.



Figure 3. Powder samples synthesized with a range of AOG ratios at 1200 °C for 12 hours. Samples are yellow-ochre, brown and black at relative high, intermediate and low cell volume respectively.

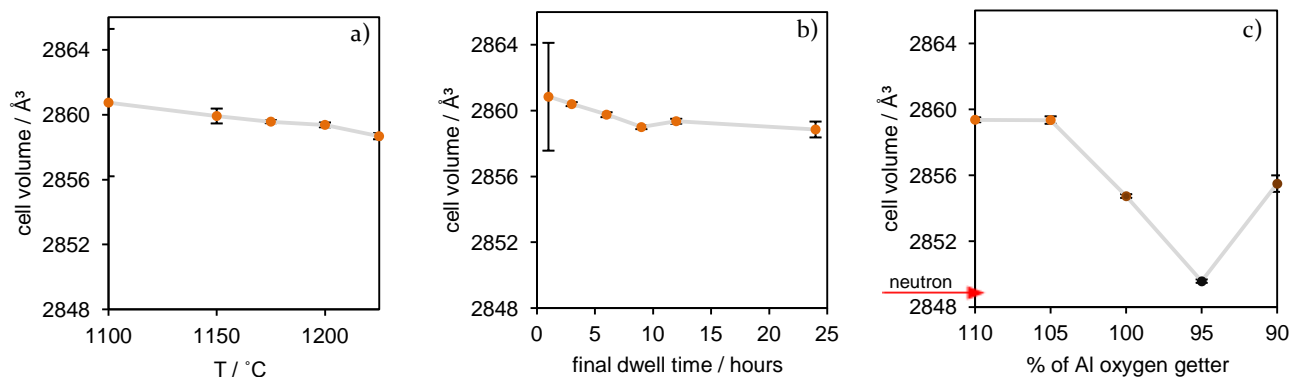


Figure 4. (a) Effect of synthesis temperature on cell volume (12 hours and 110% AOG). (b) Effect of dwell time on cell volume (1200 °C and 110% AOG). (c) Effect of AOG ratio on cell volume (12 hours, 1200 °C). The red arrow indicates the cell volume of the sample prepared for NPD experiments. The color of data symbols represents sample color. Cell volumes are refined from XRPD data using a $\sim 28.4 \text{ \AA} \times 5.7 \text{ \AA} \times 17.7 \text{ \AA}$ unit cell in space group $Imcb$, which is later shown to be the correct space group.

The most likely cause of the contraction in cell volume is the partial oxidation of Ce from +3 to +4. This effect has been seen in the related compound $\text{CeOCu}_{1-x}\text{S}$, which has been studied by several different groups.^{11,25,26} Charge compensation in this system is achieved via loss of Cu^{1+} , with reported samples ranging from near stoichiometric CeOCuS (dark olive green) to $\text{CeOCu}_{0.762}\text{Se}$ (jet black), with a reduction in cell volume of around 5%. If $\text{Ce}_2\text{O}_2\text{ZnSe}_2$ charge compensates via loss of Zn^{2+} , the Zn loss is expected to be significantly lower. Firstly, the reduction in cell volume is only around 0.4% in $\text{Ce}_2\text{O}_2\text{ZnSe}_2$ between the highest and lowest cell volumes synthesized. Secondly, the loss of only one Zn^{2+} ion is required to compensate for the oxidation of two Ce atoms. We can speculate that as the cell volume reduction in $\text{Ce}_2\text{O}_2\text{ZnSe}_2$ is less than 10% that observed in

$\text{CeOCu}_{0.762}\text{Se}$, and as Zn^{2+} loss can compensate for the oxidation two Ce atoms, the lowest cell volume sample would have a Zn content of >0.98 . Further support that this contraction is caused by partial oxidation of Ce comes from our ongoing work on solid solutions of various $\text{Ln}_2\text{O}_2\text{MSe}_2$ -type phases. We find that changing the lanthanide leads to an approximately isotropic change in all lattice parameters, whereas substitution of M leads to a change mainly in the c direction, perpendicular to the layers. This is attributed to a relatively rigid Ln-O layer and a more flexible M-Se layer which adapts to the size demands of the Ln-O layer. Figure 5 shows the relative changes in cell parameters as a function of AOG quantity, when refined in the correct orthorhombic cell, space group $Imcb$ with unit cell dimensions of $\sim 28.4 \text{ \AA} \times \sim 5.7 \text{ \AA} \times \sim 17.7 \text{ \AA}$.

The change of all cell parameters by roughly equal amounts as AOG quantity is reduced suggests a contraction occurs in the Ln-O layer, as expected for partial oxidation of the Ce, and that this dominates over Zn²⁺ loss in the more flexible M-Se layer.

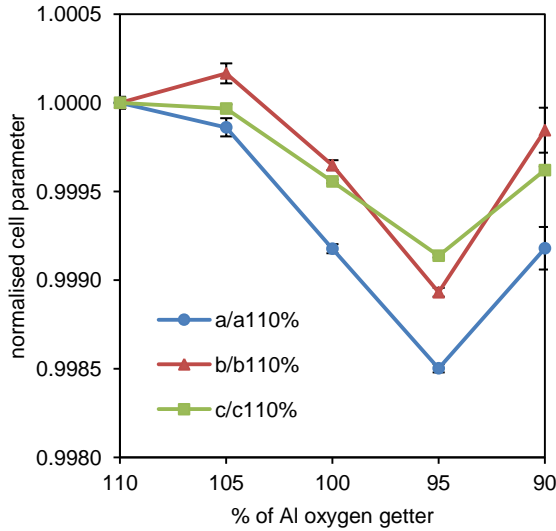


Figure 5. Effect of AOG molar quantity on normalized cell parameters.

Superstructure Investigation

Selected area electron diffraction (SAED) images were collected on the black, low cell volume NPD sample, Figure 6, and confirm the presence of the superstructure reflections suggested from the PXRD patterns. Intense reflections consistent with the parent $P4/nmm$ parent structure are labeled in white in Figure 6b; weak superstructure reflections are observed along $[1\bar{1}0]$ and indexed in green. These are not present along $[110]$, suggesting the tetragonal symmetry has been lost. Figure 6c shows $[110]$ zone axis data. It reveals no superstructure reflections along $[001]$ or $[110]$, only reflections consistent with the parent structure are observed.

SAED images of $\text{La}_2\text{O}_2\text{ZnSe}_2$ ¹⁵ revealed similar superstructure reflections, also exclusively along $[1\bar{1}0]$, though at $\frac{1\bar{1}}{44}0$, $\frac{1\bar{1}}{22}0$, and $\frac{3\bar{3}}{44}0$. These additional reflections were indexed as 200, 400, $h00$ ($h = 2n$) in a $4\sqrt{2}a_{\text{subcell}} \times \sqrt{2}a_{\text{subcell}} \times 2c_{\text{subcell}}$ unit cell. It therefore seemed likely that the $\text{Ce}_2\text{O}_2\text{ZnSe}_2$ structure may be related to the $P4/nmm$ parent by a $5\sqrt{2}a_{\text{subcell}} \times \sqrt{2}a_{\text{subcell}} \times 2c_{\text{subcell}}$ unit cell. To confirm this supercell, Pawley refinements were attempted in the orthorhombic space group $P222$ with unit cell dimensions $\sim 28.35 \text{ \AA} \times \sim 5.67 \text{ \AA} \times \sim 17.71 \text{ \AA}$. This unit cell successfully accounts for all observed reflections in the powder data of the black, low cell volume NPD sample.

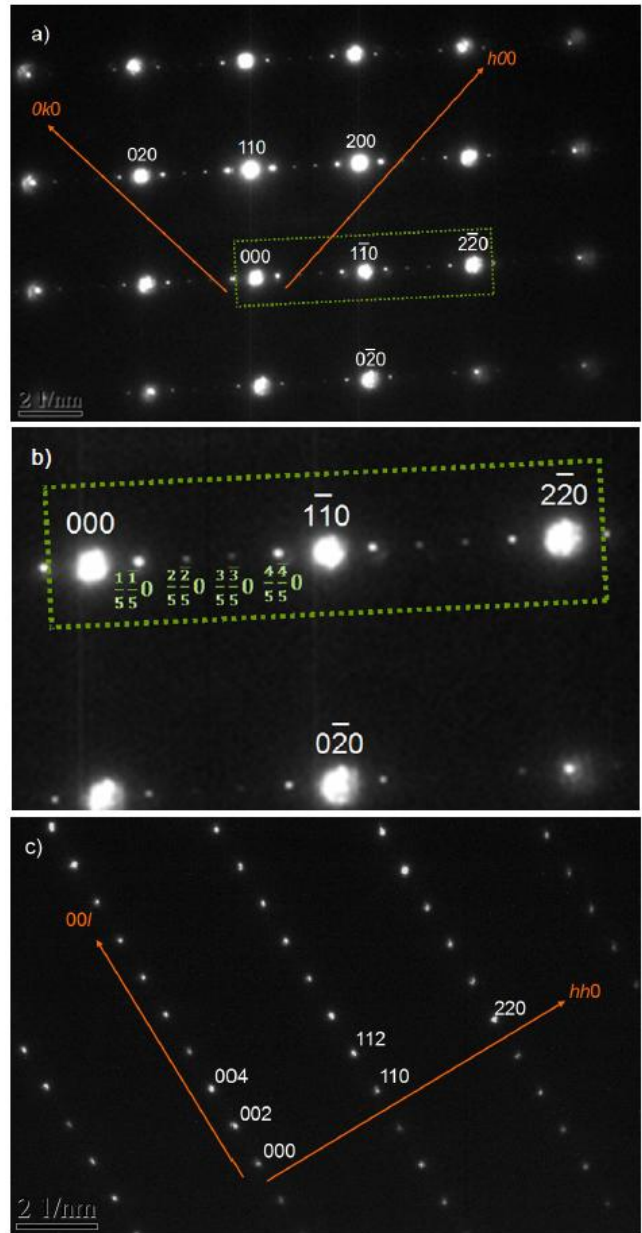


Figure 6. Selected area electron diffraction of $\text{Ce}_2\text{O}_2\text{ZnSe}_2$ taken down the (a) $[001]$ zone axis, (b) enlarged $[001]$ zone axis showing superstructure reflections, (c) $[110]$ zone axis. Zone axes and hkl indices are given relative to the parent $P4/nmm$ tetragonal cell. Reflections consistent with the parent structure are labeled white, superstructure reflections are labeled green.

Development of the Crystal Structure Model

The crystal structure was solved with the help of the web-based ISODISTORT software.²⁷ ISODISTORT calculates symmetry adapted distortion modes (displacive, site ordering, magnetic) associated with irreducible representations at different k -points. A low symmetry structure can then be described in terms of the parent structure and the amplitudes of the different ordering and displacive symmetry modes. This allows systematic and rapid exploration of different daughter structures from a given parent.

Compared to the parent, electron diffraction shows supercell diffraction peaks at $(1/5 \ 1/5 \ g)$, Figure 6b and Pawley

refinement confirms that they can be explained with a $5\sqrt{2}a_{\text{subcell}} \times \sqrt{2}a_{\text{subcell}} \times 2c_{\text{subcell}}$ cell. The distortion vector of $\text{Ce}_2\text{O}_2\text{ZnSe}_2$ relative to the parent structure is therefore $S(\alpha \alpha 1/2)$ with $\alpha = 1/5$ or $1/10$ (due to systematic absences) and the representative basis is (supercell):

$$\begin{bmatrix} 5 & 5 & 0 \\ -1 & 1 & 0 \\ 0 & 0 & 2 \end{bmatrix} \begin{bmatrix} a_{\text{subcell}} \\ b_{\text{subcell}} \\ c_{\text{subcell}} \end{bmatrix} = \begin{bmatrix} a_{\text{supercell}} \\ b_{\text{supercell}} \\ c_{\text{supercell}} \end{bmatrix}$$

There are 16 possible daughter models within 6 space groups: $Cmca$ (S_1 or S_3), $Cmca$ (S_1, S_2, S_3 or S_4), $Ccca$ (S_2 or S_4) when $\alpha = 1/5$ and $Imma$ (S_1 or S_3), $Ibam$ (S_1, S_2, S_3 or S_4), $Ibca$ (S_2 or S_4) when $\alpha = 1/10$. Refinements were performed (on the XRPD data of the black, low cell volume NPD sample) for each of these 16 daughter models in which the amplitudes of S ordering and displacive modes were refined. The effect on the R_{wp} of the refinement is shown in Figure 7.

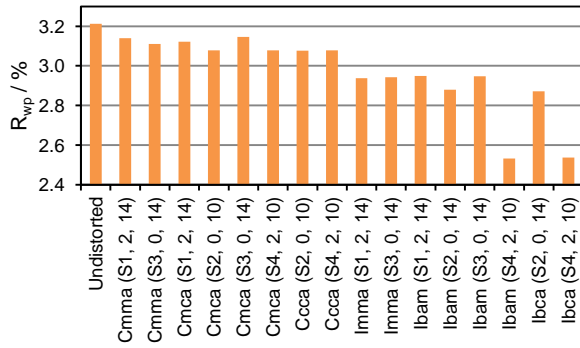


Figure 7. Refined R_{wp} for the $\text{Ce}_2\text{O}_2\text{ZnSe}_2$ XRPD pattern using different distorted models. The values in brackets give the specific S distortion mode label and the number of refined primary ordering and displacive modes.

There are two distorted models based on S_4 distortions, $Ibam$ (72) and $Ibca$ (73), which give significantly better agreement with the experimental data than others, both with $R_{\text{wp}} = 2.53\%$. The ordering patterns of the Zn-Se layer in these two space groups are in Figure 8. In an $Ibam$ (S_4) model, Zn^{2+} sites can be either fully occupied or fully vacant while in the $Ibca$ (S_4) model, there is one Wyckoff site 50% occupied by Zn^{2+} (shown as a half sphere in Figure 8b).

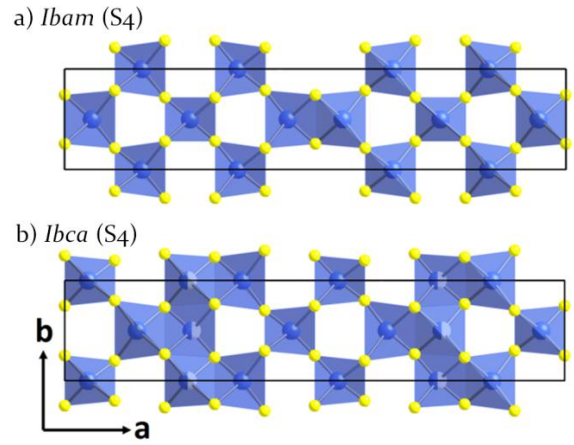


Figure 8. Zn ordering patterns in the Zn-Se layer of $\text{Ce}_2\text{O}_2\text{ZnSe}_2$ for (a) $Ibam$ and (b) $Ibca$ models from ISODISTORT refinement. Zn^{2+} cations are shown in blue and Se^{2-} anions are shown in yellow. The 50% occupied site is shown as a half sphere.

These two models are mathematically different though experimentally difficult to distinguish, even from “Rietveld quality” ($14 \text{ h } 8\text{-}120^\circ 2\theta$) laboratory powder diffraction data. Simulations show that the largest difference in the X-ray data between the two models should be the 110 reflection at $\sim 16.4^\circ 2\theta$, with an intensity of $\sim 0.25\%$ of the most intense peak; this peak is systematically absent in the $Ibca$ model. A 54 hr scan over a 2θ range of $15\text{-}21^\circ 2\theta$ was therefore collected; this reveals weak intensity for the 110 reflection (Figure 9). A good fit to these limited data was achieved using the Rietveld-derived model discussed below. We therefore selected the ordered $Ibam$ (S_4) model for final Rietveld refinement.

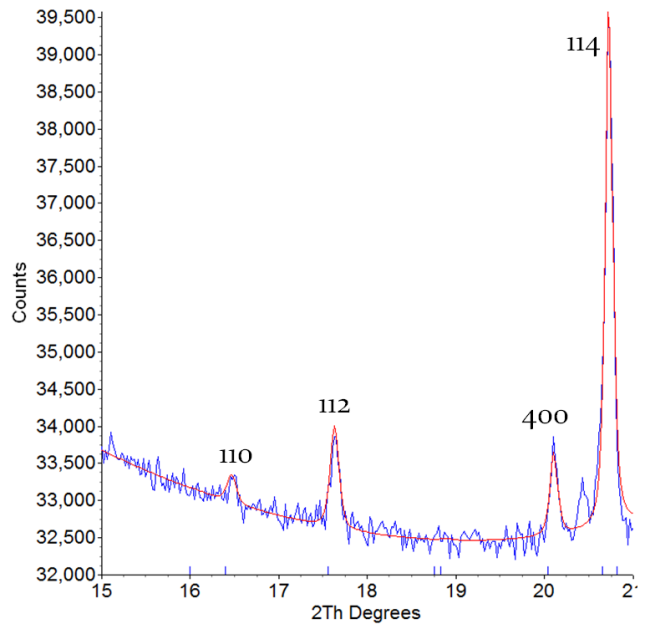


Figure 9. Rietveld refinement profile of $\text{Ce}_2\text{O}_2\text{ZnSe}_2$ XRPD data (54 hr scan over 2θ range $15\text{-}21^\circ$) fitted using the ordered $Ibam$ model. Data are consistent with an $\sim 0.25\%$ intensity 110 reflection. The very weak peak at $\sim 20.5^\circ$ is due to a $< 0.3\%$ impurity.

Structure Refinement and Description

Final Rietveld refinements were performed on the fully cation-ordered model in space group $Imcb$ (non-standard

setting of *Ibam* with the *c*-axis perpendicular to the layers for consistency with other structures of this type reported in the literature), against X-ray and neutron powder data of the black, low cell volume PND sample; a total of 209 parameters were refined. Refinement of a single O, Zn and Se site occupancy gave a sample composition of $\text{Ce}_2\text{O}_2\text{ZnSe}_2$ within 3 standard uncertainties, hence no indication of partial occupancy of Zn as charge compensation for partial Ce^{4+} formation can be detected. All sites were therefore considered fully occupied within the quality of the data. Refining separate temperature factors for each site did not significantly reduce the R_{wp} , so a single temperature factor was refined for each atom type. Structural parameters are shown in Table 1. Selected Rietveld plots are shown in Figure 10 (all refinement profiles can be found in Fig S12 of the supporting information). Selected bond lengths and angles are shown in section 3 and 4 of the supporting information respectively. Figure 11 illustrates the structure of $\text{Ce}_2\text{O}_2\text{ZnSe}_2$.

$\text{Ce}_2\text{O}_2\text{ZnSe}_2$ contains fluorite-like $[\text{Ce}_2\text{O}_2]^{2+}$ layers of Ce_4O tetrahedra, alternating with anti-fluorite-like $[\text{ZnSe}_2]^{2-}$ layers, perpendicular to the *c* axis of the material. It is closely related to the LnOCuCh -type structure, except the divalent nature of Zn^{2+} leads to half occupancy of the tetrahedral sites within the transition metal selenide layers.

The transition metal ordering pattern adopted in $\text{Ce}_2\text{O}_2\text{ZnSe}_2$ is novel, yet closely related to other divalent transition metal containing compounds. It contains both edge-sharing and corner-sharing ZnSe_4 tetrahedra, leading to alternating “checkerboard-like” and “stripe-like” regions along the *a* axis.

This is similar to the $\text{La}_2\text{O}_2\text{ZnSe}_2$ structure,¹⁵ except $\text{Ce}_2\text{O}_2\text{ZnSe}_2$ has an extended checkerboard section. Using a simple nomenclature we can describe the Ce material as 4C-1E and La as 3C-1E. Both $\text{Ce}_2\text{O}_2\text{ZnSe}_2$ and $\text{La}_2\text{O}_2\text{ZnSe}_2$ can therefore be considered as intermediate structures between $\text{Ce}_2\text{O}_2\text{FeSe}_2$,¹³ where all cations order in stripes of edge-sharing tetrahedra (oC-1E), and $\text{La}_2\text{O}_2\text{CdSe}_2$,¹⁴ where all cations order in a checkerboard arrangement (1C-oE) of corner-sharing tetrahedra.

While Zn ordering is the main driver for the symmetry lowering, there are significant accompanying structural distortions, mainly in the Zn–Se tetrahedra shown in Figure 12 and Figure 13. These are most pronounced in the edge-shared Zn_1Se_4 tetrahedra and reduce on moving from Zn_2Se_4 tetrahedra to Zn_3Se_4 in the centre of the corner-sharing block. As expected, the Zn–Zn separation in the edge-shared tetrahedra is significantly longer than an idealized structure [3.13(3) vs ~ 2.84 Å]. Similar distortions are observed in the Zn–Se tetrahedra of $\text{La}_2\text{O}_2\text{ZnSe}_2$, where the edge-shared Zn–Zn separation is even greater (3.22 Å).¹⁵ The distortions in the OCe_4 tetrahedra are less pronounced, though still considerable. This is most evident in the O_1Ce_4 tetrahedron, which lies below the centre of the corner-sharing block where ZnSe_4 tetrahedra are least distorted. A distortion-mode analysis (see supplementary information 5 and 6) shows that the 4 most significant structural distortions are S_4 modes on Zn ([100] direction), Se, Ce and O (all [010] direction).

Table 1. Structural parameters of $\text{Ce}_2\text{O}_2\text{ZnSe}_2$ from combined refinement using room temperature XRPD and NPD data. Space group *Imcb*, $a = 28.3595(4)$ Å, $b = 5.67087(8)$ Å, $c = 17.71308(6)$ Å; $R_{wp} = 1.848\%$, $R_p = 1.081\%$ and $\chi^2 = 1.193$. Occupancy for all sites is 1.

Site label	Wyckoff site	<i>X</i>	<i>y</i>	<i>z</i>	<i>B</i> / Å ²	Valence
Ce(1)	16k	0.1992(3)	0.741(1)	0.3191(4)	0.47(2)	3.19
Ce(2)	16k	0.3998(3)	0.770(1)	0.3188(4)	0.47(2)	3.26
Ce(3)	8j	0	0.777(1)	0.8200(6)	0.47(2)	3.16
O(1)	8g	0.75	0	0.2560(4)	0.63(3)	2.24
O(2)	16k	0.8504(3)	0.486(3)	0.2499(2)	0.63(3)	2.41
O(3)	16k	-0.0501(4)	-0.025(2)	0.2517(3)	0.63(3)	2.31
Zn(1)	8i	0.0551(3)	0.5	0	1.19(3)	1.76
Zn(2)	8h	0.1515(4)	0	0	1.19(3)	1.96
Zn(3)	4b	0.75	0	0.5	1.19(3)	2.03
Se(1)	16k	0.7002(4)	0.254(1)	0.0831(3)	0.87(2)	1.82
Se(2)	16k	0.8991(3)	0.2305(8)	0.0878(2)	0.87(2)	1.85
Se(3)	8j	0	0.725(1)	0.0845(5)	0.87(2)	1.77

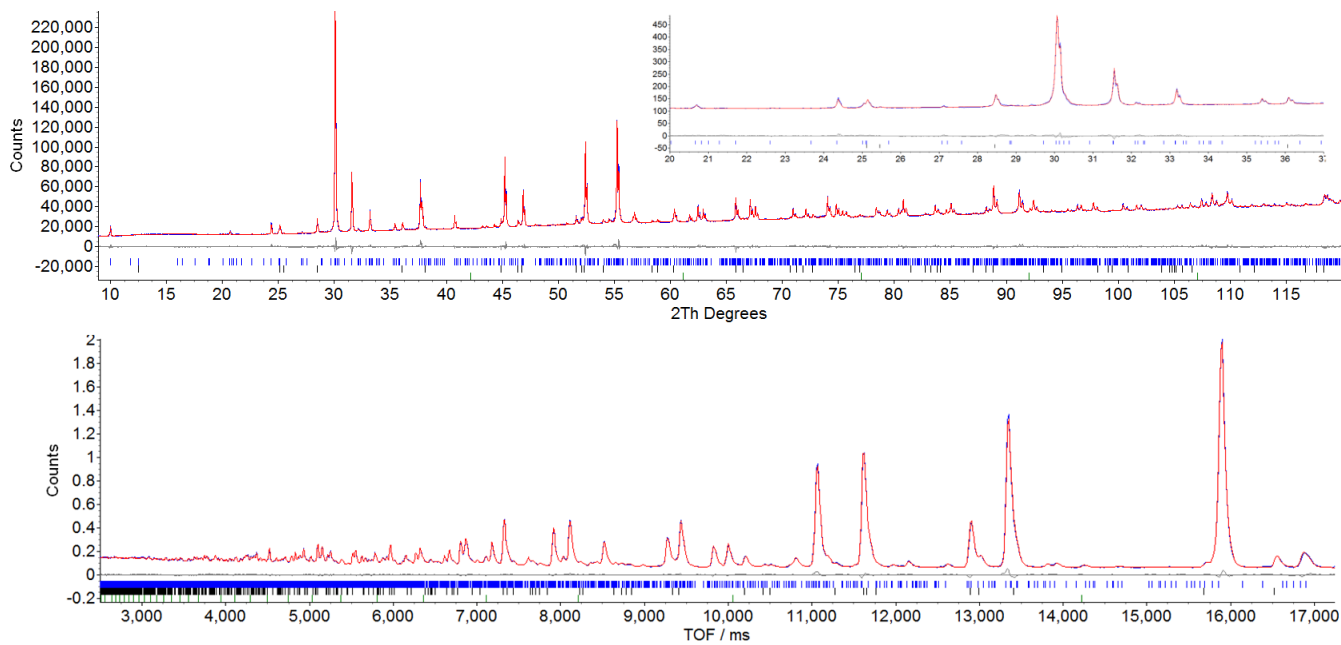


Figure 10. Rietveld refinement profiles from combined refinement using room-temperature (top) XRPD and (bottom) NPD data for $\text{Ce}_2\text{O}_2\text{ZnSe}_2$. Tick marks show reflection positions for $\text{Ce}_2\text{O}_2\text{ZnSe}_2$ (blue ~95% by weight), $\text{Ce}_2\text{O}_2\text{Se}$ (black ~5% by weight) and vanadium (green, from sample can used in PND data collection).

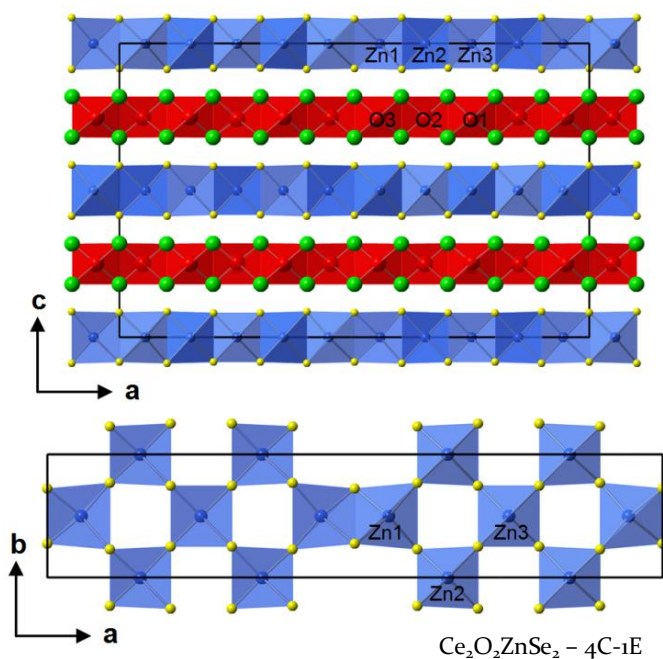


Figure 11. (Top) $\text{Ce}_2\text{O}_2\text{ZnSe}_2$ structure with sheets of edge-sharing Ce_2O (red) and ZnSe_4 tetrahedra (blue), viewed down $[010]$. (Bottom) view down $[001]$ showing a mix of stripe-like edge-sharing ZnSe_4 tetrahedra and checkerboard-like corner-sharing ZnSe_4 tetrahedra (4C-1E), with an extended checkerboard-like section relative to $\text{La}_2\text{O}_2\text{ZnSe}_2$.

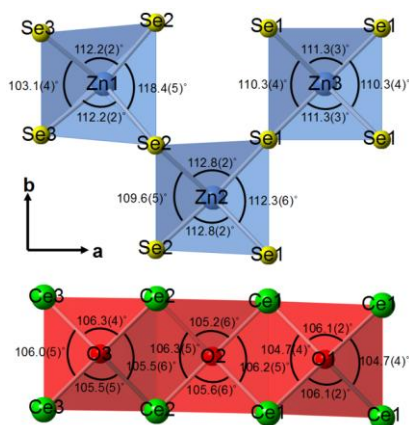


Figure 12. Coordination environments of Zn and O sites viewed down $[001]$.

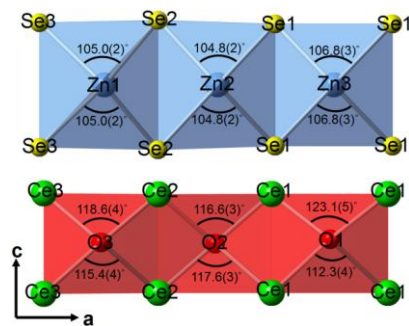


Figure 13. Coordination environments of Zn and O sites viewed down $[010]$.

Cell Volume Dependence of the Zinc Ordering Pattern

The model presented above describes most of the $\text{Ce}_2\text{O}_2\text{ZnSe}_2$ samples synthesised; however it describes those with lower cell volume better than those with higher cell volume. Figure 14a shows the XRPD patterns of the sample synthesised with a 3 h final dwell at 1200 °C and 10% AOG molar amount. This is the highest cell volume sample synthesised with sufficient phase purity (>95%) to clearly observe superstructure reflections. The structural model does not accurately describe the superstructure reflections.

Figure 14b-d show the XRPD patterns of the samples synthesised with 105%, 100% and 95% AOG respectively (all at 1200 °C for 12 hours), which represent samples with systematically decreasing cell volume (Figure 4c). The structural model provides a progressively better fit to superstructure reflections as the cell volume decreases. Figure 14e shows the XRPD patterns of the sample synthesised for NPD experiments, which has the lowest cell volume and gives an excellent fit to the structural model presented.

On-going work suggests that superlattice peaks in samples (a) to (d) are incommensurately modulated peaks due to a size mismatch between $[\text{Ce}_x^{4+}\text{Ce}_{2-x}^{3+}\text{O}_2]^{(2+x)+}$ and zinc selenide layers. For the low cell volume sample (e) this locks in to the commensurate structure presented.

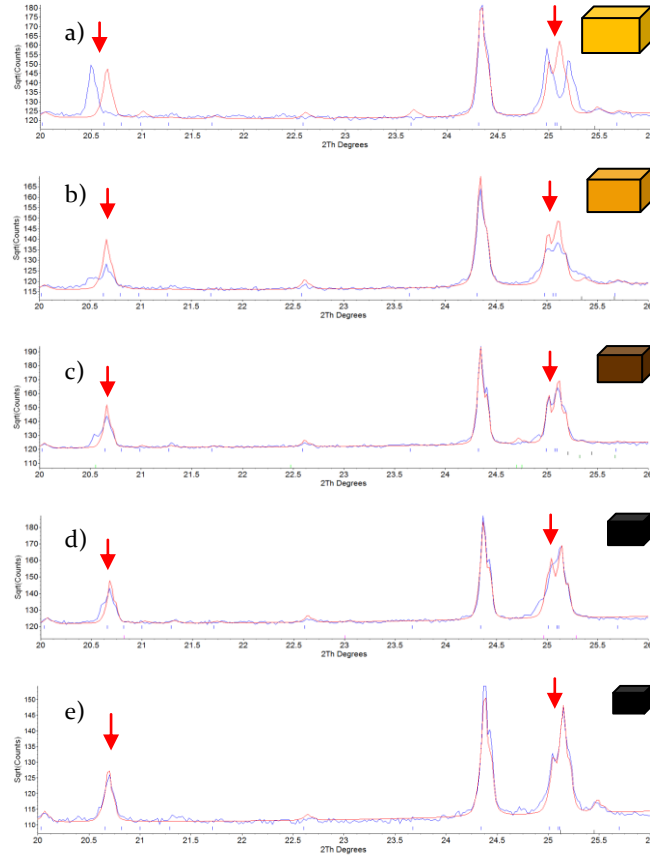


Figure 14. Rietveld fits of XRPD patterns of $\text{Ce}_2\text{O}_2\text{ZnSe}_2$ samples with systematically decreasing cell volume from (a) to (e), as shown by the cuboids, the color of which shows the sample colour. The structural model proposed provides a good fit to superstructure reflections (marked by red arrows) for the minimum cell volume samples.

Diffuse Reflectance Spectroscopy

Diffuse reflectance spectroscopy (DRS) reveals different band gaps for high, intermediate and low-cell volume $\text{Ce}_2\text{O}_2\text{ZnSe}_2$

samples, which is unsurprising based on their different colors. The high-cell volume yellow ochre sample, intermediate-cell volume brown sample and low-cell volume black sample have band gaps of ~ 2.2 eV, ~ 1.4 eV and ~ 1.3 eV respectively, as shown in Figure 15. The narrowing of the band gap is not linearly dependant on cell volume. Measured band gaps are significantly smaller than for $\text{La}_2\text{O}_2\text{ZnSe}_2$ (~ 3 eV),¹⁵ and are strongly influenced by Ce(IV) content.

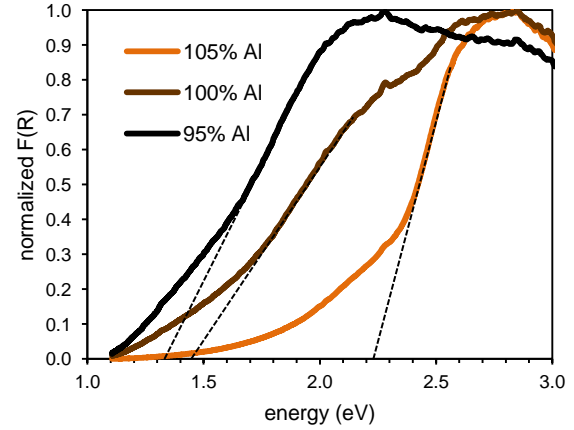


Figure 15. Normalized diffuse reflectance spectra after Kubelka-Munk treatment for $\text{Ce}_2\text{O}_2\text{ZnSe}_2$ samples synthesised with 105% AOG (yellow), 100% AOG (brown) and 95% AOG (black), showing interband transitions corresponding to an optical band gap of ~ 2.2 eV, ~ 1.4 eV and ~ 1.3 eV respectively.

Magnetic Properties

The temperature dependence of the molar magnetic susceptibility (χ_{mol}) of $\text{Ce}_2\text{O}_2\text{ZnSe}_2$ (NPD sample) is shown in Figure 16. $\text{Ce}_2\text{O}_2\text{ZnSe}_2$ is a typical paramagnet, and obeys the Curie-Weiss law from 150 K to 300 K. By Curie-Weiss fitting $1/\chi_{\text{mol}} - T$ data from 150 -300 K, we obtain an effective magnetic moment of $\text{Ce}_2\text{O}_2\text{ZnSe}_2$ of $\mu_{\text{eff}} = 3.43(1) \mu_{\text{B}}$, which equates to $\mu_{\text{eff}} = 2.42(1) \mu_{\text{B}}$ for each $\text{CeOZn}_{0.5}\text{Se}$. In $\text{Ce}_2\text{O}_2\text{ZnSe}_2$, the magnetic properties come from the $4f$ open shell ion Ce^{3+} . The ground state of Ce^{3+} is $^2F_{5/2}$ with a theoretical effective magnetic moment $\mu_{\text{eff}} = 2.54 \mu_{\text{B}}$, however, most experiment results of Ce^{3+} show $\mu_{\text{eff}} \sim 2.4 \mu_{\text{B}}$.²⁸ The Weiss constant Θ is $-10(2)$ K indicating local antiferromagnetic interactions, however we do not observe the onset of long range order down to 2 K. Similar behaviour has been reported for $\text{Ln}_4\text{O}_4\text{Se}_3$ ($\text{Ln} = \text{Ce}$ and Nd) systems.²⁹

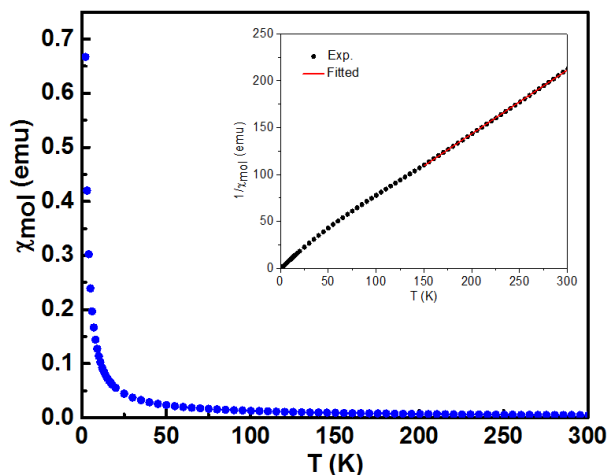


Figure 16. Molar susceptibility of $\text{Ce}_2\text{O}_2\text{ZnSe}_2$ at different temperatures.

CONCLUSION

We describe here the synthesis, structural characterization, optical measurements and magnetic measurements of the new material $\text{Ce}_2\text{O}_2\text{ZnSe}_2$. It adopts a ZrCuSiAs -related structure with ordering of Zn^{2+} cations over the tetrahedral sites in the $[\text{ZnSe}_2]^{2-}$ layers. The ordering pattern contains both corner-sharing and edge-sharing tetrahedra and is intermediate between ordering patterns observed for $\text{Ce}_2\text{O}_2\text{FeSe}_2$ and $\text{La}_2\text{O}_2\text{CdSe}_2$. It is similar to $\text{La}_2\text{O}_2\text{ZnSe}_2$ except that $\text{Ce}_2\text{O}_2\text{ZnSe}_2$ has extended corner-shared regions. The color of the compound changes as a function of cell volume, which varies by $\sim 0.4\%$. At the highest, intermediate and lowest cell volume the color is yellow-ochre, brown and black respectively. This decrease is attributed to partial oxidation of the Ce from +3 to +4, the extent of which can be controlled by the synthetic conditions.

$\text{Ce}_2\text{O}_2\text{ZnSe}_2$ is a semiconductor in all cases with experimental optical band gaps of 2.2, 1.4 and 1.3 eV for the samples colored yellow ochre, brown and black respectively. SQUID measurements show $\text{Ce}_2\text{O}_2\text{ZnSe}_2$ to be paramagnetic down to 2 K.

ASSOCIATED CONTENT

Rietveld refinement profiles for refinement of ZrCuSiAs structural model for $\text{Ce}_2\text{O}_2\text{ZnSe}_2$; Rietveld refinement profiles for *Imcb* model; bond lengths; bond angles; table of occupancy mode number, atom type, mode label, *k*-point and order parameter direction; histogram showing the most significant structural distortions; a cif file of the final refinement. This material is available free of charge via the Internet at <http://pubs.acs.org>.

AUTHOR INFORMATION

Corresponding Author

*E-mail: john.evans@durham.ac.uk

ACKNOWLEDGEMENTS

We thank ISIS for neutron time. We are grateful to Dr. Budhika Mendis for assistance during electron diffraction measurements, Andrew Duckworth for assistance with DRS

measurements and Dr. Johan Buurma for SQUID measurements. We thank EPSRC for funding.

REFERENCES

- (1) Kamihara, Y.; Watanabe, T.; Hirano, M.; Hosono, H. *J. Am. Chem. Soc.* **2008**, *130*, 3296-3297.
- (2) Mizuguchi, Y.; Fujihisa, H.; Gotoh, Y.; Suzuki, K.; Usui, H.; Kuroki, K.; Demura, S.; Takano, Y.; Izawa, H.; Miura, O. *Phys. Rev. B* **2012**, *86*, 5.
- (3) Singh, S. K.; Kumar, A.; Gahtori, B.; Shruti; Sharma, G.; Patnaik, S.; Awana, V. P. S. *J. Am. Chem. Soc.* **2012**, *134*, 16504-16507.
- (4) Tan, S. G.; Li, L. J.; Liu, Y.; Tong, P.; Zhao, B. C.; Lu, W. J.; Sun, Y. P. *Physica C: Superconductivity* **2012**, *483*, 94-96.
- (5) Yazici, D.; Huang, K.; White, B. D.; Chang, A. H.; Friedman, A. J.; Maple, M. B. *Philosophical Magazine* **2012**, *93*, 673-680.
- (6) Krzton-Maziopa, A.; Guguchia, Z.; Pomjakushina, E.; Pomjakushin, V.; Khasanov, R.; Luetkens, H.; Biswas, P. K.; Amato, A.; Keller, H.; Conder, K. *J. Phys-condens. Mat.* **2014**, *26*, 5.
- (7) Phelan, W. A.; Wallace, D. C.; Arpino, K. E.; Neilson, J. R.; Livi, K. J.; Seabourne, C. R.; Scott, A. J.; McQueen, T. M. *J. Am. Chem. Soc.* **2013**, *135*, 5372-5374.
- (8) Sathish, C. I.; Feng, H. L.; Shi, Y. G.; Yamaura, K. *J. Phys. Soc. Jpn.* **2013**, *82*, 6.
- (9) Ueda, K.; Inoue, S.; Hirose, S.; Kawazoe, H.; Hosono, H. *Appl. Phys. Lett.* **2000**, *77*, 2701-2703.
- (10) Hiramatsu, H.; Yanagi, H.; Kamiya, T.; Ueda, K.; Hirano, M.; Hosono, H. *Chem. Mater.* **2007**, *20*, 326-334.
- (11) Ueda, K.; Takafuji, K.; Hiramatsu, H.; Ohta, H.; Kamiya, T.; Hirano, M.; Hosono, H. *Chem. Mater.* **2003**, *15*, 3692-3695.
- (12) Ijjaali, I.; Mitchell, K.; Haynes, C. L.; McFarland, A. D.; Van Duyne, R. P.; Ibers, J. A. *J. Solid State Chem.* **2003**, *176*, 170-174.
- (13) McCabe, E. E.; Free, D. G.; Evans, J. S. O. *Chem. Commun.* **2011**, *47*, 1261-1263.
- (14) Hiramatsu, H.; Ueda, K.; Kamiya, T.; Ohta, H.; Hirano, M.; Hosono, H. *J. Mater. Chem.* **2004**, *14*, 2946-2950.
- (15) Tuxworth, A. J.; McCabe, E. E.; Free, D. G.; Clark, S. J.; Evans, J. S. O. *Inorg. Chem.* **2013**, *52*, 2078-2085.
- (16) Rietveld, H. M. *J. Appl. Crystallogr.* **1969**, *2*, 65.
- (17) Coelho, A. A. *J. Appl. Crystallogr.* **2003**, *36*, 86-95.
- (18) Coelho, A. A. *TOPAS Academic: General Profile and Structure Analysis Software for Powder Diffraction Data*, 5th ed.; Bruker AXS: Karlsruhe, Germany, 2012.
- (19) Coelho, A. A.; Evans, J. S. O.; Evans, I. R.; Kern, A.; Parsons, S. *Powder Diffr.* **2011**, *26*, S22-S25.
- (20) Dollase, W. *J. Appl. Crystallogr.* **1986**, *19*, 267-272.
- (21) Pitschke, W.; Hermann, H.; Mattern, N. *Powder Diffr.* **1993**, *8*, 74-83.
- (22) Kortum, G.; Braun, W.; Herzog, G. *Agnew. Chem., Int. Ed.* **1963**, *2* (7), 333-404.
- (23) Tandon, S. P.; Gupta, J. P. *Phys. Status Solidi* **1970**, *38*, 363-367.
- (24) Benacerraf, A.; Guittard, M.; Domange, L.; Flahaut, J. *Bull. Soc. Chim. Fr.* **1959**, 1920-1922.
- (25) Chan, G. H.; Deng, B.; Bertoni, M.; Ireland, J. R.; Hersam, M. C.; Mason, T. O.; Van Duyne, R. P.; Ibers, J. A. *Inorg. Chem.* **2006**, *45*, 8264-8272.
- (26) Pitcher, M. J.; Smura, C. F.; Clarke, S. J. *Inorg. Chem.* **2009**, *48*, 9054-9056.
- (27) Campbell, B. J.; Stokes, H. T.; Tanner, D. E.; Hatch, D. M. *J. Appl. Crystallogr.* **2006**, *39*, 607-614.
- (28) Frederikse, H. P. R. In *CRC handbook of chemistry and physics*; 84th ed.; Lide, D. R., Ed.; CRC Press: 2004, p 12-117.
- (29) Strobel, S.; Choudhury, A.; Dorhout, P. K.; Lipp, C.; Schleid, T. *Inorg. Chem.* **2008**, *47*, 4936-4944.

For Table of Contents Only

We report the synthesis and characterisation of the new oxyselenide $\text{Ce}_2\text{O}_2\text{ZnSe}_2$ which contains fluorite-like $[\text{Ce}_2\text{O}_2]^{2+}$ layers of Ce_4O tetrahedra (red), alternating with anti-fluorite-like $[\text{ZnSe}_2]^{2-}$ layers (blue). The Zn ordering pattern in the selenide layers is novel, yet closely related to other divalent transition metal containing compounds. $\text{Ce}_2\text{O}_2\text{ZnSe}_2$ contains both edge- and corner-sharing ZnSe_4 tetrahedra, leading to alternating “checkerboard-like” and “stripe-like” regions along the a axis.

